AFRL-OSR-VA-TR-2014-0300

REACTIVE COLLISIONS AND INTERACTIONS OF ULTRACOLD DIPOLAR ATOMS

Svetlana Kotochigova
TEMPLE UNIVERSITY-OF THE COMMONWEALTH SYSTEM OF HIGHER EDUCA

10/29/2014
Final Report

Air Force Research Laboratory
AF Office Of Scientific Research (AFOSR)/ RTB
Arlington, Virginia 22203
Air Force Materiel Command

REPORT DOCUMENTATION PAGE

Form Approved
OMB No. 0704-0188

PLEASE DO NOT RETURN YOUR FORM TO THE ABOVE ORGANIZATION.

1. REPORT DATE *(DD-MM-YYYY)*	2. REPORT TYPE	3. DATES COVERED *(From - To)*
27-10-2014	Final report	From 15 AUG 2011 to 14 NOV 2014

4. TITLE AND SUBTITLE
Reactive Collisions and Interactions of Ultracold Dipolar Atoms

5a. CONTRACT NUMBER

5b. GRANT NUMBER
FA9550-11-1-0243

5c. PROGRAM ELEMENT NUMBER

6. AUTHOR(S)
Dr. Svetlana Kotochigova

5d. PROJECT NUMBER

5e. TASK NUMBER

5f. WORK UNIT NUMBER

7. PERFORMING ORGANIZATION NAME(S) AND ADDRESS(ES)
Temple University, Physics Department
1900 N. 13th Street, Philadelphia, PA 19122-6082

8. PERFORMING ORGANIZATION REPORT NUMBER

9. SPONSORING/MONITORING AGENCY NAME(S) AND ADDRESS(ES)
Dr. Tatjana Curcic
Program Officer, Atomic and Molecular Physics
Air Force Office of Scientific Research/RTB
875 North Randolph St.
Arlington, VA 22203, (703)696-6204 tatjana.curcic.1@us.af.mil

10. SPONSOR/MONITOR'S ACRONYM(S)

11. SPONSOR/MONITOR'S REPORT NUMBER(S)

12. DISTRIBUTION/AVAILABILITY STATEMENT
There is no limitation on the distribution of this report. Distribution A

13. SUPPLEMENTARY NOTES

14. ABSTRACT

We explored Feshbach resonances in the collision between ultracold highly-magnetic dysprosium and erbium atoms. The resonance density is orders of magnitude larger than seen in any other previously studied atomic system. Moreover, we showed that these resonance can only exist because of the anisotropic nature of the atom-atom potentials. Analysis of nearest-neighbor spacings between Feshbach resonances shows a chaotic distribution that one would expect from random-matrix theory. We explained these statistics as originating from the large strength of the anisotropy.

We demonstrated that the vibrational motion of BaCl+ molecules is quenched by collisions with ultracold calcium atoms at a rate comparable to the Langevin rate. This is over four orders of magnitude more efficient than traditional sympathetic cooling schemes. In addition, we calculated the electronic structure of BaCl+ and other molecular ions. Based on these results we found unusually-large rates for cold charge-transfer reactions between neutral and ionic atoms.

15. SUBJECT TERMS
ultracold atoms and molecules, dynamic polarizability, Feshbach resonances, magnetic atoms, laser control of molecules

16. SECURITY CLASSIFICATION OF:			17. LIMITATION OF ABSTRACT	18. NUMBER OF PAGES	19a. NAME OF RESPONSIBLE PERSON
a. REPORT	b. ABSTRACT	c. THIS PAGE			19b. TELEPHONE NUMBER *(Include area code)*
U	U	U			

Reset

Final Progress Report to AFOSR, award No. FA9550-11-1-0243

Reactive Collisions and Interactions of Ultracold Dipolar Atoms

Svetlana Kotochigova

Department of Physics, Temple University, Philadelphia, PA 19122-6082

I. COLLISIONAL INTERACTIONS OF RARE-EARTH MAGNETIC ATOMS

The breakthroughs in the experimental realization of the strongly correlated quantum gases of atoms with a large magnetic moments, such as Cr [1], Dy [2, 3], and Er [4], open a new scientific playground for the study of quantum magnetism with high-spin atomic systems. This new research area comes into play due to long-range anisotropic nature of interactions between these magnetic atoms that allows to engineer exotic many-body phases with control and tunability. Due to its large spin, dipolar gases of magnetic atoms represent an excellent environment for exploring the interface between condensed matter and atomic physics, as recently illustrated by [5], where the complex spin dynamics observed for doubly-occupied sites of the Cr lattice. Models of quantum magnetism were also engineered with polar molecules based on the anisotropic nature of their field-induced long-range interactions.

We studied the collision between magnetic Dysprosium (Dy) and Erbium (Er) atoms, of interest for several ongoing experiments [2–4, 6, 7]. Dy and Er have a ground-state configuration with an unfilled inner 4f shell shielded by a closed $6s^2$ outer shell. In the 4f-shell electrons are spin aligned with an orbital angular momentum that is maximal. Hence, these atoms have very large magnetic moments, $10\mu_B$ in Dy and $7\mu_B$ in Er, and a large total angular momentum leading to anisotropic magnetic and dispersion interaction potentials between the atoms.

We first studied, classified, and constructed the atom-atom interaction potentials. This included a coupled-cluster calculation of some of the short-range electronic potentials when the electron-clouds of the atoms overlap, as well as a determination of the anisotropic dispersion, magnetic dipole-dipole, and electric quadrupole-quadrupole interaction when the atoms are further apart [8]. Secondly, we set up a close-coupling calculation combining these interactions and predicted scattering cross-sections as function of collision energy as well as magnetic field B.

We succeeded in calculating C_6 van-der-Waals coefficients for both species, based on known atomic transition frequencies and oscillator strengths. As an example, Figure 1 shows our results for Er as a function of the projection Ω of the total molecular angular momentum $\vec{J}$ on the interatomic axis. Details for Dy+Dy and Er+Er calculations can be found in Refs. [8, 9].

The spin structure of the 4f shell leads to 153 potentials for Dy and 91 for Er dissociating to the ground state limit. We assumed that the ratios of the *ab-initio* potentials are the same as for their adiabatic C_6 coefficients. Consequently, we could construct all potentials requiring only a coupled-cluster calculation for the single *gerade* potential with maximal projection Ω and knowledge of the van der Waals coefficients. As an initial model this approach is justified, as the bond is mainly due to the overlap of the isotropic $6s^2$ shells.

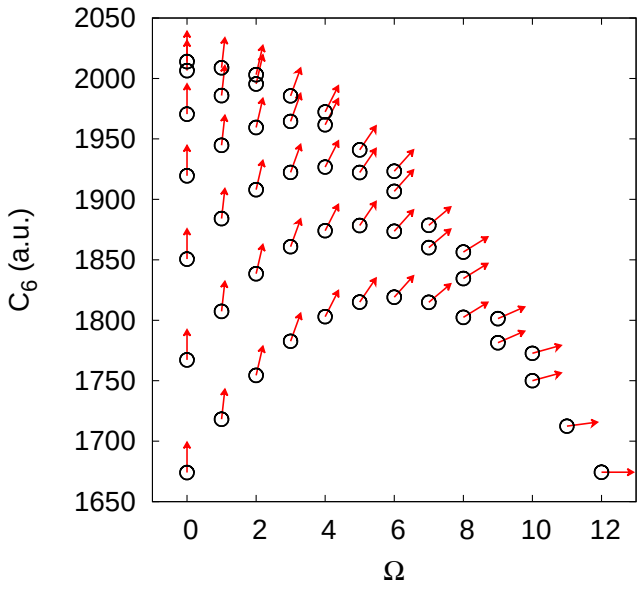

FIG. 1: *Gerade* adiabatic dispersion coefficients in atomic units for two ^{3}H$_6$ Er atoms as a function of the projection Ω of the total angular momentum $\vec{J}$ on the interatomic axis. Arrows symbolize the orientation of $\vec{J}$.

We also determined the strength of the quadrupole-quadrupole (q-q) interaction, based on a coupled-cluster calculation of the atomic quadrupole moments. The moments are small, with $Q = -0.00524$ a.u. for Dy and Q=0.0289 a.u. for Er, leading to a q-q interaction that can be safely neglected.

The next step was setting up a coupled-channel calculation, allowing atoms to rotate and vibrate and where the atomic Zeeman states are coupled by the anisotropic interactions. The calculations were performed with the symmetrized channels $|j_1 m_1\rangle|j_2 m_2\rangle Y_{\ell m}(\hat{R})$ with projections m_i of the atomic angular momentum along the magnetic field direction. The spherical harmonic $Y_{\ell m}(\hat{R})$ describes rotation with partial wave ℓ and anisotropic interactions couple channels between different ℓ. A description of our closed-coupling calculation for Dy atoms can be found in [10] and for Er in [11].

A first-principle coupled-channel model allowed us to calculate anisotropy-induced magnetic Feshbach-resonance spectra of bosonic atoms. The model treats the Zeeman, magnetic dipole-dipole, and isotropic and anisotropic dispersion interactions on equal footing. The Hamiltonian includes

$$H = -\frac{\hbar^2}{2\mu_r}\frac{d^2}{dR^2} + \frac{\vec{\ell}^2}{2\mu_r R^2} + H_Z + V(\vec{R},\tau),$$

where $\vec{R}$ describes the orientation of and separation between the two atoms. The first two terms are the radial kinetic and rotational energy operators, respectively. The Zeeman interaction is $H_Z = g\mu_B(j_{1z}+j_{2z})B$, where g is an atomic g-factor and j_{iz} is the z component of the angular momentum operator $\vec{j}_i$ of atom $i = 1, 2$. The nuclear repulsion, $V(\vec{R},\tau)$, is anisotropic and τ labels the electronic variables. Finally, μ_r is the reduced mass and for $R \to \infty$ the interaction $V(\vec{R},\tau) \to 0$. A magnetic field B is aligned along the $\hat{z}$ direction. Coupling between the basis states is due to $V(\vec{R},\tau)$.

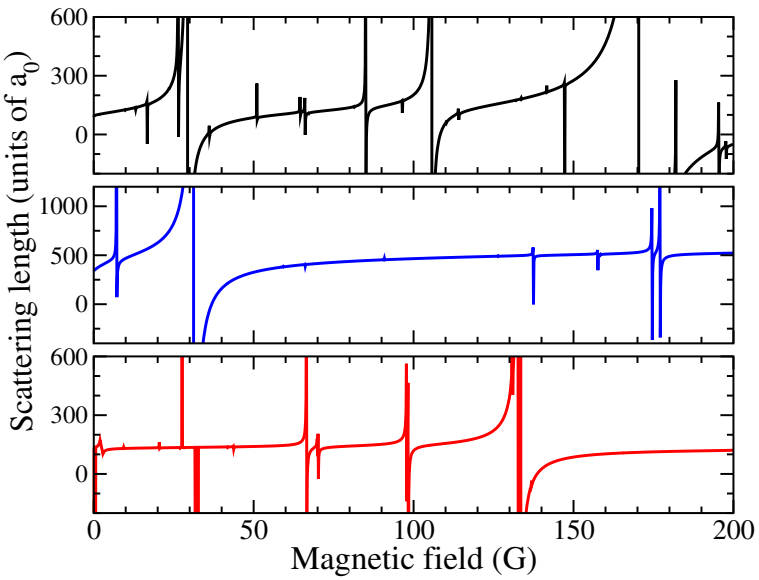

FIG. 2: Scattering length of $m=-8$ ^{164}Dy atoms in Bohr radii as a function of magnetic field with and without the magnetic dipole-dipole or the anisotropic contribution of the dispersion interaction. We use a collision energy of E/k =30 nK and channels with even partial waves $\ell \leq 10$. The top panel shows the case when all interactions are included. In the middle and bottom panel the dispersion and magnetic dipole-dipole anisotropy are set to zero, respectively.

Figure 2 shows the scattering length for the collision of two stretched $m = -8$ ^{164}Dy atoms as a function of B. The calculation included 91 channels with even $\ell \leq 10$. We observed a large number of resonances, many are narrow, some are broad, that can only exist because of the anisotropic interactions between the atoms. These "anisotropic" resonances for submerged shell atoms differ from those in alkali-metal atom collisions. For alkalis the hyperfine interaction between electron and nuclear spins gives sufficient complexity, without coupling partial waves, that resonances occur without anisotropy.

We have also performed coupled-channels calculations for Er+Er scattering in the basis $|j_1 m_1, j_2 m_2, \ell m_\ell\rangle \equiv Y_{\ell m_\ell}(\theta,\phi)|j_1 m_1\rangle|j_2 m_2\rangle$, where $\vec{j}_{a=1,2}$ are the atomic angular momenta with space-fixed projection $m_{a=1,2}$ along the magnetic field direction, spherical harmonics $Y_{\ell m_\ell}(\theta,\phi)$ describe molecular rotation with partial wave $\vec{\ell}$, and angles θ and ϕ orient the internuclear axis relative to the magnetic field. In this basis the Zeeman and rotational interaction are diagonal and coupling between the basis states is due to 91 molecular Born-Oppenheimer (BO) potentials and the magnetic dipole-dipole interaction. The BO potentials induce either isotropic (ℓ and m_ℓ conserving) or anisotropic (ℓ or m_ℓ changing) couplings. The Hamiltonian conserves $M_{\rm tot} = m_1 + m_2 + m_\ell$ and couples only even (odd) ℓ. For fixed $M_{\rm tot}$ simulations are made tractable by only including basis states with $0 \leq \ell \leq L_{\rm max}$.

For homonuclear collisions only basis states with even $j + \ell$ exist. We have used $M_{\rm tot} = -16$ and even $\ell \leq 20$. Figure 3 shows the elastic rate coefficients for collisions between two m = -6 ^{168}Er atoms in range of magnetic field strength from zero to 50 Gauss. The temperature is chosen to be 360 nK.

Both theoretical simulation data show a large number of overlapping Feshbach resonances. We have performed an analyses of the distribution of magnetic field separations between

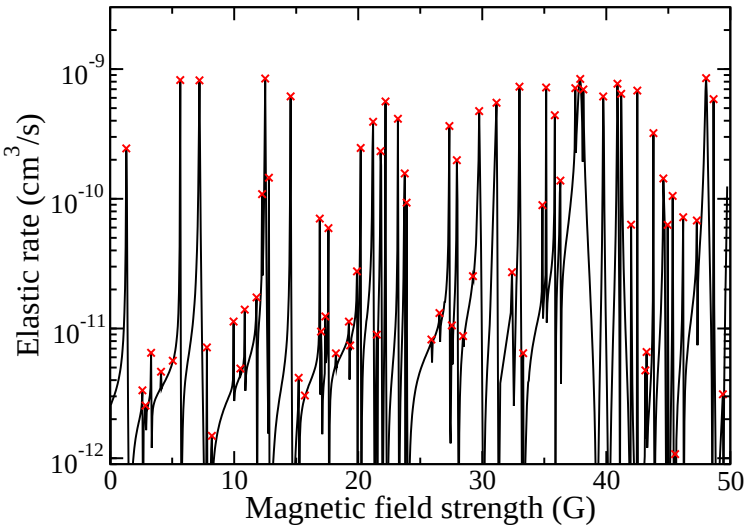

FIG. 3: Elastic rate coefficient of $m = -6$ ^{168}Er collisions as a function of magnetic field using a collision energy of $E/k = 360$ nK. Partial waves ℓ up to 20 are included.

neighboring Feshbach resonances and compare to similar analyses of the experimental data [11]. Results of our statistical analyses are presented in Fig. 4. This figure shows the distribution of the nearest-neighbor spacings (NNS) between Feshbach resonances for the ^{168}Er isotope for fields between B=30 G to 70 G and grouping resonance spacings ΔB in bins with a width of 160 mG. These spacings scaled to the mean spacing, s, were then

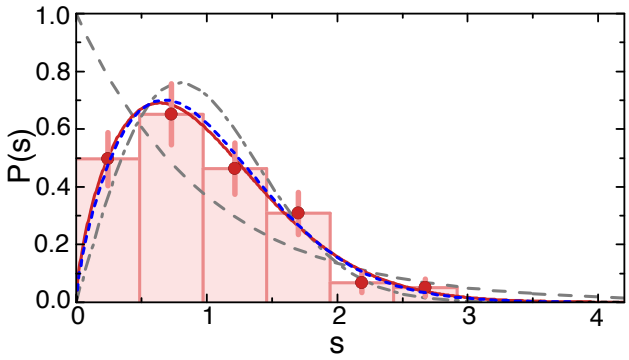

FIG. 4: The normalized distribution $P(s)$ of nearest-neighbor spacings (NNS) of ^{168}Er Feshbach resonances as a function of dimensionless $s = \Delta B\bar{\rho}$, where the ΔB are NNS and $\bar{\rho}$ is the mean resonance density per unit field strength. The experimental data is shown as a bar graph and filled red circles with error bars. The dash gray, dash-dotted gray, and solid red curves are Poisson, Wigner-Dyson, and Brody distributions fit to the experimental data, respectively. The dashed blue line is a Brody distribution fit to the distribution of NNS of a close-coupling calculation where partial waves up to $L_{\max} = 20$ have been included.

fit to a Poisson distribution $P(s) = \exp(-s)$ for non-interaction levels, the Wigner-Dyson distribution $P(s) = (\pi/2)s\exp(-\pi s^2/4)$ characterizing strongly interacting levels, and the Brody distribution, which is a one-parameter function that smoothly connects between the Poisson and Wigner-Dyson distribution. The distribution is similar in shape as for the experimental data. Both distributions are fit by the Brody distribution with $\eta = 0.6$, which favors Wigner distribution.

II. COLLISIONAL COOLING AND DETECTION OF IONIC MOLECULES

Sympathetic cooling of molecular ions by collisions with laser-cooled atoms was predicted to be efficient at cooling the internal molecular degrees of freedom [12]. Although the prediction relied on proven technologies, it was not previously implemented, possibly owing to the misconception that molecular ions predominantly undergo charge-exchange reactions leading to energetic, neutral molecules. The PI was involved in the first realization of sympathetic cooling of trapped $BaCl^+$ in collisions with Ca atoms co-located in a magneto-optical trap [13]. The experiment was performed in the group of Dr. E. Hudson at UCLA.

Evaluation of how well molecular ions are cooled was crucial. We relied on state-sensitive photodissociative detection of $BaCl^+$ to ionic Ba^+ and neutral Cl atoms, shown schematically in Fig. 5a. This method is applicable to any molecule that can be photodissociated as long as the internal state can be probed within the vibrational relaxation time. The method exploits the fact that, although the photodissociation cross-section is broad, the individual vibrational levels have unique frequency responses for photodissociation. It is, however, necessary to measure the photodissociation cross-section with high precision.

We supplied accurate electronic potentials and dipole moments for $BaCl^+$, shown in Fig. 5a and b, and created the quantum-mechanical model of the photodissociation cross sections. These simulations determined the cross section of individual vibrational states; the lowest two of which (that is, $v = 0$ and $v = 1$) are shown in Fig. 5c. Assuming a Maxwell-Boltzmann distribution for the vibrational populations, a fit to the experimental signal gave the internal temperature.

Our theoretical research also gave insight into charge exchange between Ca and Yb^+ [14]. We first determined the previously unknown potential surfaces that dissociate to the nearly-degenerate $Ca+Yb^+$ and Ca^++Yb limits as well as the transition dipole moment between these potentials see Fig. 6. For these calculations we used a non-relativistic multi-configurational second-order perturbation theory (CASPT2) implemented in the MOLCAS software suite. This approach works exceptionally well for the structure of this molecule where the potential surfaces dissociating to the $Ca(3s^2)+Yb^+(6s)$ and $Ca^+(3s)+Yb(6s^2)$ limits are energetically close. The reference wave functions are obtained from a complete active space self consistent field (CASSCF) calculation. The TZVP quality ANO-RCC basis set of the valence space consists of the 9s 8p 4d 3f 2g orbitals for Ca and 6s 5p 3d 2f 1g orbitals for Yb. The potential curves relevant to the experimental observation have solid lines and are labeled $X^2\Sigma^+$ and $A^2\Sigma^+$ for the two ground states of the molecular ions spectroscopic constants are presented in Figure 6.

We then developed quantum mechanical models for three charge-exchange channels: non-radiative transfer, radiative transfer, and radiative association, and calculated the rate coefficients for each. The two potentials of Fig. 6 are closest at 15 a.u. The interaction allows for the non-radiative charge exchange, which we calculate using a coupled-channel (cc) method.

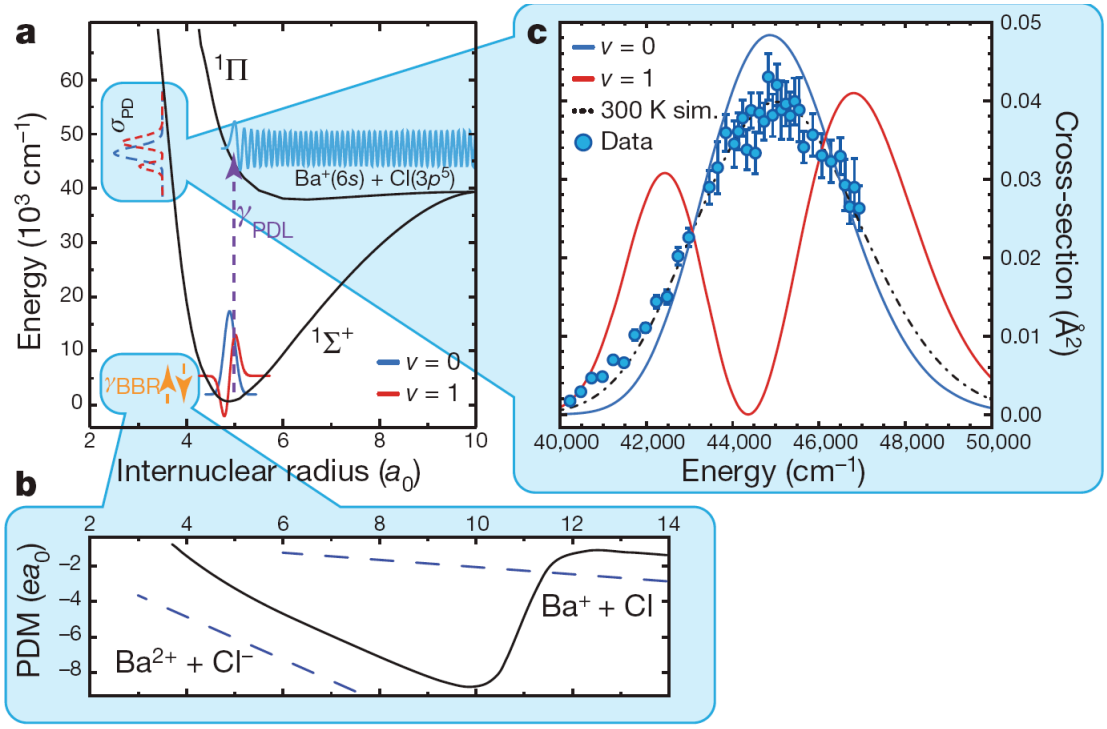

FIG. 5: State-sensitive photodissociation of $BaCl^+$. a) The $X^1\Sigma^+$ and $A^1\Pi$ potential curves as functions of internuclear separation and an arrow indicating the photodissociation pathway. The $v=0$ and $v=1$ vibrational states have different frequency responses to the laser. b) Permanent dipole moment of the $X^1\Sigma^+$ state. c) Experimental and theoretical cross-section of the photodissociation transition. The dash-dot line is a thermally averaged cross section at 300 K. Also shown are the $v=0$ and $v=1$ contributions.

Since we have initially two particles colliding (Yb^+ and Ca) they do not bind together. Therefore we are looking at the non-radiative charge exchange transition (nRT) from a continuum state to a continuum state. In order to do the cc calculation we first diabatized the potentials shown by the red dotted lines on the graph. That means that we create potentials that cross at 15 a.u. The coupling between potential, we assume to be a Lorentzian in R with the maximum value equal to half the splitting at R=15 a.u. The width of the coupling matrix element (dashed line) is chosen such that if we diagonalize the 2x2 potential matrix at each R it approximately reproduce the original potentials. To calculate the nRT rate we include many partial waves for both continua. For example, the temperatures up to 1 K require $\sim$ 100 partial waves in the calculation. Unthermalized sample has shape resonances due to the many partial waves that contribute. However, once we thermalize the effect of resonances is less visible. We also have preliminary results for the radiative rate coefficients by spontaneous emission.

To explore a role of the excited states in the charge-exchange reaction we performed extensive calculation the electronic structure of the $BaCa^+$ molecule,using a relativistic multi-reference restricted active space configuration-interaction (RMR-RAS-CI) method [15]. Spin-orbit effects are large in $BaCa^+$ and a relativistic calculation is required. A nonorthogonal basis set is constructed from numerical Dirac-Fock atomic orbitals as well as relativistic

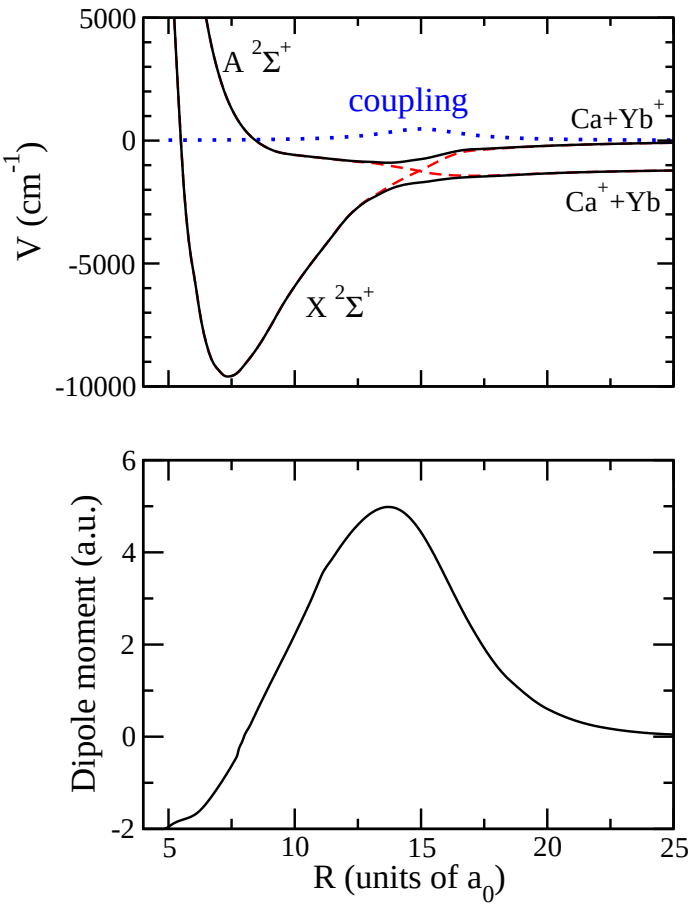

FIG. 6: Potential energy curves of the $BaCl^+$ molecule as a function of the internuclear separation R. Solid, labeled curves indicate the potentials that are involved in the photodissociation scheme. Other $^1\Sigma^+$ ($^1\Pi$) potentials are shown by dashed (dash-dotted) lines. The vertical arrow indicates the $A^1\Pi \leftarrow X^1\Sigma^+$ single-photon photodissociation transition.

Sturmian functions. A symmetric reexpansion of atomic orbitals from one atomic center to another simplifies the calculation of many-center integrals. At large interatomic separations the molecular wave function has a pure atomic form that appropriately describes the molecular dissociation limit. The $1s^22s^22p^6...4d^{10}$ closed shells of barium and $1s^22s^22p^6$ closed shells of calcium atom are included in the core. An R-dependent all-electron core potential is calculated exactly and included in the Hamiltonian. The core-valence basis set is constructed from Dirac-Fock core $5s$ and $5p$ orbitals for Ba and $3s$ and $3p$ orbitals for Ca. Valence Dirac-Fock orbitals are $6s$, $5d$, and $6p$ for Ba and $4s$, $3d$, and $4p$ for Ca, while Sturm virtual $7s$, $7p$, $6d$, $8s$ $8p$ and $7d$ orbitals for Ba and $5s$, $5p$, $4d$, $6s$, $6p$, and $5d$ orbitals for Ca are also included. We have tentitatively indicated which potentials correspond to entrance and exit channels in the reactions that occur in UCLA experiment [16]. Loss only

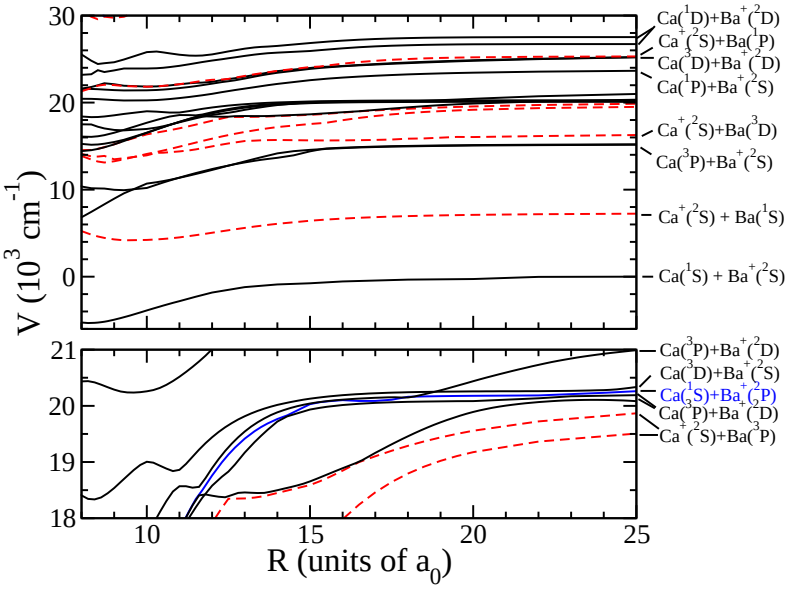

FIG. 7: Potential energies of the Ω=1/2 excited states of the $BaCa^+$ molecule as a function of interatomic separation R. The zero of energy is at the ground-state dissociation limit. The entrance channel (solid lines) and exit channels (dashed lines) potentials are shown over an energy range of 16×10^3 cm^{-1}. The bottom panel shows higher detail for potentials above the $Ca^+(^2S)$+$Ba(^1D)$ dissociation limit.

occurs to exit channels with an asymptotic energy that is lower than that of the entrance channel. The main reason for calculating the Ω=1/2 potentials is that only they are seen in the experiment. The lowest-excited Born-Oppenheimer potentials of Ω=1/2 symmetry for this calculation are shown in Fig. 7. The curves are also assigned by their atomic dissociation limit. The entrance channel potentials are shown by solid lines and exit channels are plotted by dashed lines. In the energy range around 20×10^3 cm^{-1} of the dissociations energy the potential curves are closely spaced. It shows that there are strong interactions or avoided crossings between neighboring excited potentials. Potentials that dissociate to an energy larger than 27×10^3 cm^{-1} are not shown. Coupling between potentials are due to radial non-adiabatic couplings. A coupled-channels calculation that includes these mixings falls outside the scope of this study.

A. Reactive scattering and trapping of ultracold neutral molecules

Recent experiments with ultracold KRb molecules in their absolute ground state have shown evidence for short-range chemical reactions [17]. In these experiments molecules were allowed to collide with each other or with remaining cold atoms. At ultracold temperatures these collisions are governed by quantum-mechanical threshold effects. Measurements of the inelastic collision rate for KRb+K found a rate of $1.7(3) \times 10^{-10}$ cm^3/s, which is primarily due to a reaction to K_2+Rb.

This first experimental effort could only probe the total loss rates. Similarly, the first

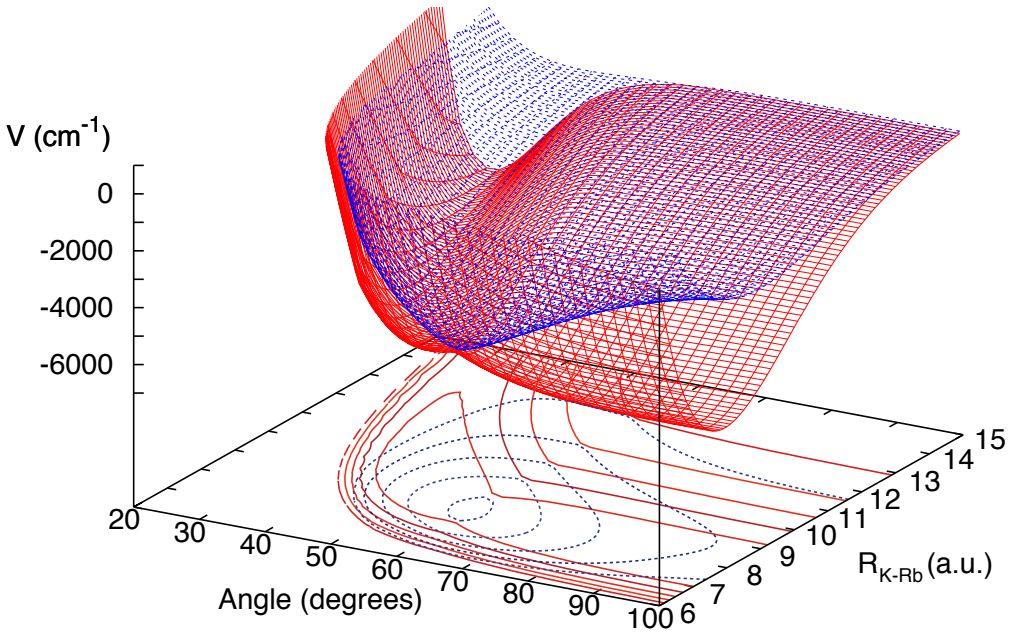

FIG. 8: Potential energy surfaces of the three-atomic K_2Rb system in the C_{2v} symmetry as functions of the KRb separation and angle between K-Rb-K.

theoretical models [18, 19] based on "simple" quantum-defects ideas could only determine the total loss rate. It would, however, be beneficial to obtain state-to-state reaction rates. From the theory side this will require a multi-channel scattering calculation of the reaction as well as a determination of the three-body potential surfaces.

We started our investigation of the KRb + K to K_2+ Rb reaction by obtaining the potential surfaces of this three-atomic system using the MOLCAS package. We obtained the lowest two doublet K_2Rb potentials and found, for example, that at the absolute lowest energy Rb is separated by $8.24a_0$ and $10.4a_0$ from the two K atoms with an angle of 48.4° between K-Rb-K. The dissociation energy of the lowest doublet potential is $E/(hc) = 1915$ cm^{-1} to K_2+ Rb, while its atomization energy to three free atoms is 5740 cm^{-1}. The two doublet-spin potentials dissociate to the same atomization limit and, in addition, have a conical intersection for the C_{2v} symmetry, where the separation R_{RbK} between Rb and each of the K atoms is the same. Figure 8 shows this conical intersection for the potentials.

As a next step we incorporated the potentials into a multi-channel quantum-defect theory for three-atomic systems (the statistical model) [20] to approximately solve the three-particle Schrödinger equation. The model assumes the existence of a long-lived trimer resonance with all three atoms close together, decaying incoherently into reagent and reactant products. In our context, reagent and reactant products correspond to rovibrational levels of the KRb and K_2 dimer, respectively. The multi-channel aspect of the statistical theory indicates the exact coupled-channels treatment of the couplings between the reagent (reactant) ro-vibrational levels due to the presence of the third atom.

In addition, we studied the dynamic polarizability of the $N = 0$ and $N = 1$ rotational levels of the $v = 0$ vibrational level of the ground $X^1\Sigma^+$ state of KRb [21]. The molecules are placed in a 1063 nm optical dipole trap and exposed to an external magnetic field B of 545.9 G. There is no static external electric field present. We extend the ideas of mix-

ing of rotational levels due a static external electric field of Ref. [19] to include mixing of rotational-hyperfine levels due to intrinsic nuclear electric-quadrupole interactions introduced in Ref. [22]. The goal is to theoretically determine the polarizability of the selected $|N, m_N, m_{\rm K}, m_{\rm Rb}\rangle$ rotational-hyperfine levels and describe their dependence on the angle θ between the direction of the magnetic field and the polarization of the optical trapping lasers. Here N describes the rotational quantum number, m_N, $m_{\rm K}$ and $m_{\rm Rb}$ are projections of $\vec{N}$ and the nuclear spin $\vec{I}_a$ of $a = {\rm K}$ and Rb onto the external magnetic-field axis, respectively.

First, we construct the full Hamiltonian for these rotational-hyperfine levels. It includes the nuclear Zeeman interaction, $-\mu_a I_{\rm z,a} B$ for atom $a = {\rm K}$ or Rb, where the magnetic field is along the z direction and μ_a is the nuclear magneton of atom a. It also includes the nuclear quadrupole interaction, $(eqQ)_a C_2(\theta\phi) \cdot T_2(I_a, I_a)$, with coupling constants $(eqQ)_a$ for each atom a that couples its nuclear spin to rotational states. Here, $C_{lm}(\theta\phi)$ is a spherical harmonic and $T_{2m}(I_a, I_a)$ is a rank-2 tensor created from the spin I_a. Finally, we include a polarizability interaction Hamiltonian, $-(\alpha_\parallel \mathcal{O}_\parallel + \alpha_\perp \mathcal{O}_\perp) I$, with strengths $\alpha_\parallel$ and $\alpha_\perp$, tensor operators $\mathcal{O}_\parallel$ and $\mathcal{O}_\perp$ that depend on light polarization and rotational angular momentum $\vec{N}$, and I is the laser intensity of the dipole trap.

This Hamiltonian couples $(1+3)\times 9 \times 4 = 144$ channels $|N, m_N, m_{\rm K}, m_{\rm Rb}\rangle$ and has four parameters: the quadrupole interaction constants for each of the two atoms and the "reduced" polarizabilities $\alpha_\parallel$ and $\alpha_\perp$, which are the vibrationally-averaged $v = 0$ parallel and perpendicular polarizabilities that include contributions from all excited $^1\Sigma^+$ and $^1\Pi$ potentials, respectively. We find transition energies by diagonalizing the Hamiltonian and analyzing its eigenfunctions to connect to the states that have been observed experimentally. Eigenstates are identified by the channel state with the largest contribution. Typically this contribution is more than 90% and we are justified in labeling eigenstates by one $|N, m_N, m_{\rm K}, m_{\rm Rb}\rangle$.

The two quadrupole parameters were estimated in Ref. [22] based on measurements of transition energies between sub-levels of the $N = 0$ and $N = 1$ states in the optical dipole trap. Here we improve these constants using new measurements of the transition energies for three hyperfine levels of the $N = 1$ rotational state removing the effects of the trapping psed on these fits we can now predict polarizabilities of any state of the manifold as a function of angle θ and intensity I of trapping laser field. The polarizability of eigenstate j with energy $E_j(I)$ is defined as the derivative $\alpha_j = -dE_j/dI$, evaluated at laser intensity I. Figure 9 shows the polarizability as a function of θ based on the "exact" Hamiltonian for the four states studied here and laser intensity I=2.35 kW/cm^2. The agreement with experimental observations, also shown, at the same laser intensity is satisfactory. The polarizability for $|1, -1, -4, 1/2\rangle$ deviates noticeably for large angles, while that for $|1, 0, -4, 1/2\rangle$ does so for small angles. The magic angle between the states $|0, 0, -4, 1/2\rangle$ and $|1, 0, -4, 1/2\rangle$ is located at $\theta = 49$ degrees deviating from the solution of $3\cos^2\theta - 1 = 0$ predicted in Ref. [19] in the absence of the nuclear quadrupole interaction.

Figure 9 shows the polarizability, when the off-diagonal quadrupole coupling between channels is omitted. This leads to 3×3 Hamiltonian matrices, where $|N = 1, m_n = 0, 1, -1\rangle$ channels with the same nuclear spin state are coupled by the polarizability Hamiltonian operator. The difference with the exact results is small and indicates that the off-diagonal quadrupole interaction do not lead to important corrections. However, it needs a further investigation. The difference between "exact" and "finite difference" derivatives shows that the effect of the light is non-perturbative for the laser intensities used in JILA experiment. The laser induced energy shifts can be as large as those from the nuclear quadrupole inter-

actions. Finally, Fig. 9 also shows the finite difference $(E_j(I) - E_j(I = 0))/I$ corresponding to the observable measured by parametric heating experiments [21].

[1] A. Griesmaier, J. Werner, S. Hensler, J. Stuhler, and T. Pfau, Phys. Rev. Lett. **94**, 160401 (2005).

[2] M. Lu, N. Q. Burdick, S. H. Youn, and B. L. Lev, Phys. Rev. Lett. **107**, 190401 (2011).

[3] M. Lu, N. Q. Burdick, and B. L. Lev, Phys. Rev. Lett. **108**, 215301 (2012).

[4] K. Aikawa, A. Frisch, M. Mark, S. Baier, A. Rietzler, R. Grimm, and F. Ferlaino, Phys. Rev. Lett. **108**, 210401 (2012).

[5] A. de Paz, A. C. A. Sharma, E. Maréchal, J. H. Huckans, P. Pedri, L. Santos, O. Gorceix, L. Vernac, and B. Laburthe-Tolra, Phys. Rev. Lett. **111**, 185305 (2013).

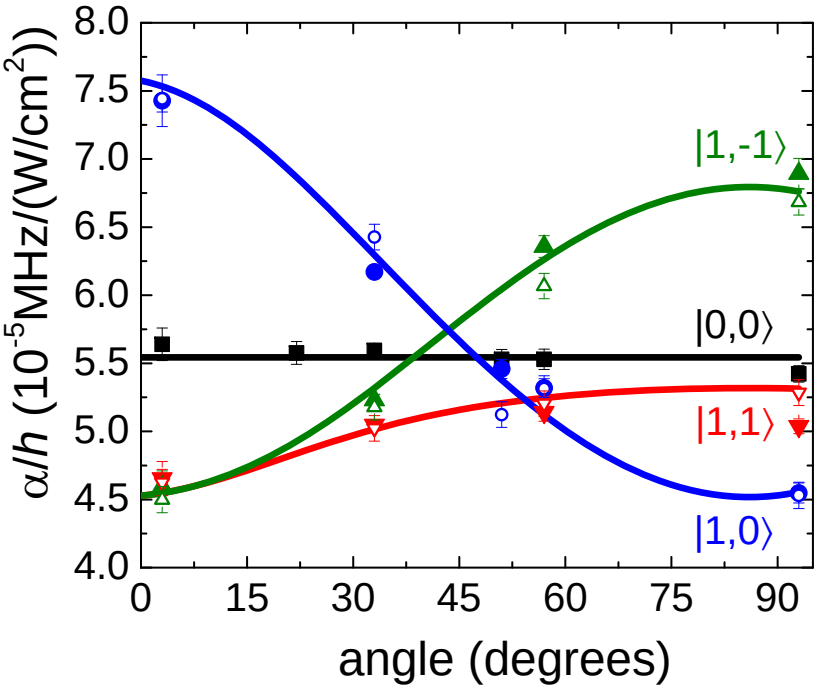

FIG. 9: Polarizability of four rotational-hyperfine states of the lowest vibrational level of the $X^1\Sigma^+$ potential of KRb as a function of angle θ between the polarization of the dipole-trap laser at 1063 nm and a bias magnetic field with strength $B = 545.9$ G. The four states are labeled by rotational levels $|N, m_N\rangle = |0, 0\rangle$ (black) , $|1, 0\rangle$ (blue), $|1, -1\rangle$ (green) and $|1, +1\rangle$ (red). We plot the finite difference Δ/I. Error bars reflect our uncertainty in locating the center of the parametric heating resonance. Open circles are a (direct) measurement of the polarizability from shifts in the microwave transition frequency. Curves are theoretical simulations of these experiments. Full curves correspond to the polarizability obtained from diagonalizing the exact Hamiltonian, dotted curves are based on the finite element form of the energy derivative, and the dashed curves are the polarizability obtained from an approximate 3×3 Hamiltonian. We only show the polarizability of the eigenstate with the most $|1, 0\rangle$ character.

[6] M. Lu, S. H. Youn, and B. L. Lev, Phys. Rev. Lett. **104**, 063001 (2009).
[7] A. Frisch, K. Aikawa, M. Mark, A. Rietzler, J. Schindler, E. Zupanic, R. Grimm, and F. Ferlaino, Phys. Rev. A **85**, 051401(R) (2012).
[8] S. Kotochigova and A. Petrov, Phys. Chem. Chem. Phys. **13**, 19165 (2011).
[9] S. Kotochigova, Rep. Prog. Phys. **77**, 093901 (2014).
[10] A. Petrov, E. Tiesinga, and S. Kotochigova, Phys. Rev. Lett. **109**, 103002 (2012).
[11] A. Frisch, M. Mark, K. Aikawa, F. Ferlaino, J. L. Bohn, C. Makrides, A. Petrov, and S. Kotochigova, Nature **507**, 475 (2014).
[12] E. R. Hudson, Phys. Rev. A **79**, 032716 (2009).
[13] W. G. Rellergert, S. T. Sullivan, S. J. Schowalter, S. Kotochigova, K. Chen, and E. R. Hudson, Nature **495**, 490 (2013).
[14] W. G. Rellergert, S. T. Sullivan, S. Kotochigova, A. Petrov, K. Chen, S. J. Schowalter, and E. R. Hudson, Phys. Rev. Lett. **107**, 243201 (2011).
[15] S. Kotochigova and E. Tiesinga, J. Chem. Phys. **123**, 174304 (2005).
[16] S. T. Sullivan, W. G. Rellergert, S. Kotochigova, and E. R. Hudson, Phys. Rev. Lett. **109**, 223002 (2012).
[17] S. Ospelkaus, K.-K. Ni, D. Wang, M. H. G. de Miranda, B. Neyenhuis, G. Quéméner, P. S. Julienne, J. L. Bohn, D. S. Jin, and J. Ye, Science **327**, 853 (2010).
[18] Z. Idziaszek and P. S. Julienne, Phys. Rev. Lett. **104**, 113202 (2009).
[19] S. Kotochigova, New J. Phys. **12**, 073041 (2010).
[20] E. Rackham, T. Gonzalez-Lezana, and D. E. Manopoulos, J. Chem. Phys. **119**, 12895 (2003).
[21] B. Neyenhuis, B. Yan, S. A. Moses, J. P. Covey, A. Chotia, A. Petrov, S. Kotochigova, J. Ye, and D. S. Jin, Phys. Rev. Lett. **109**, 230403 (2012).
[22] S. Ospelkaus, K.-K. Ni, G. Quéméner, B. Neyenhuis, D. Wang, M. H. G. de Miranda, J. L. Bohn, J. Ye, and D. S. Jin, Phys. Rev. Lett. **104**, 030402 (2010).